Applied Physics B
Lasers and Optics

CrossMark

Efficient X-ray emission from laser-irradiated low-density lead target: a substitute for gold in hohlraum design

R. Fazeli[1]

Abstract Numerical experiments are carried out to calculate continuum emissivity and opacity of plasmas produced from laser-irradiated Au and Pb targets as hohlraum wall materials. Targets are considered to be solid or porous with different initial densities. Simulation results show a good agreement compared with the measured data. The results show that under identical conditions, X-ray emission is higher for Au plasma; however, by decreasing initial densities, X-ray yield enhancement is greater for Pb plasma. By using a Pb target with initial density of about 1.14 g cm^{-3} instead of solid Au target, the same X-ray yield even more can be obtained. Calculations also show that in the conditions of solid density targets, Pb plasma offers a little lower opacity in soft X-ray region. Decreasing initial density of Pb causes its opacity to increase and get closer to the opacity of solid Au which in turn reduces energy losses in hohlraum wall.

1 Introduction

Inertial confinement fusion (ICF) is an increasingly attracting approach to gain the fusion energy all around the world. Laser or heavy ion beams can be used directly or indirectly to drive ignition by compressing a solid spherical fuel capsule (containing the deuterium and tritium fuel) to extremely high densities in a short time [1–5]. In a direct-drive technique, the laser (or heavy ion) beams are irradiated directly at the surface of the fusion pellet. But in the indirect-drive method, the laser (or heavy ion) energy is absorbed and converted into soft X-rays by a high-Z, high-opacity material at the inside walls of a cylindrical radiation cavity called "hohlraum" [5, 6]. The produced X-rays then deliver the required energy to the fuel pellet. There are some drawbacks in the direct-drive method that make it less desirable in comparison with the indirect-drive method such as hydrodynamic instabilities and sensitivity of the target to the intensity variations within each beam.

Since the late 1970s, considerable experimental and theoretical researches are performed in the area of indirect-drive physics including hohlraum physics, laser–plasma coupling, X-ray generation and transport, hydrodynamic instabilities, flux symmetry around capsules, ignition conditions, and fuel capsule physics [7–19]. One of the most critical issues is the choice of appropriate hohlraum wall materials which could offer higher X-ray conversion efficiency, lower energy loss in hohlraum walls, and lower costs and also satisfy recycling requirements. High-Z materials like gold and gold/gadolinium are widely used because of high target performance and low driver energy losses. It has been shown that mixtures of two or more materials like Au/Gd, Au/U, Au/Sm, and U/Au/Dy exhibit increased opacity (and also decreased heat capacity) in comparison with single materials [20–27]. This happens if the low opacity of a selected material in required frequency regions could be offset by the high opacity of the other one. Suter et al. [22] at NIF studied the wall losses for various one-dimensional slab of mixtures applying a Planckian radiation source to find an optimum combination. He showed that mixtures with appropriate fraction of uranium had a lower wall loss. Analytical expressions developed by Rosen and Hammer [27] showed that hohlraum walls made of low-density high-Z foams can decrease wall losses by approximately 20 %. A comparison between experiments,

✉ R. Fazeli
  rfazeli@iust.ac.ir

1 Faculty of science, Lahijan branch, Islamic Azad University, Lahijan, Iran

numerical simulations, and analytical model was reported by Jones et al. [25], which shows that a cocktail hohlraum made from a suitably chosen combination of uranium–gold–dysprosium would have about 17 % less wall losses and require about 10 % less laser energy than a gold hohlraum of the same size.

On the other hand, improving the conversion efficiency of the absorbed laser energy to the soft X-ray is another important subject in hohlraum design. Considerable works have been reported introducing methods to enhance X-ray conversion efficiency. The effects of various laser parameters such as intensity, wavelength, pulse shape, and number of pulses are explored [28, 29]. It has been shown that X-ray emission can be enhanced by using modulated surface targets [30–32], multi-layered and porous targets [33–36], and mixed-Z and gas puff targets [37, 38].

Obviously, fabrication of targets containing materials like gold, gold–gadolinium, and gold–uranium requires considerable costs. Moreover, although gold–uranium hohlraum is a good choice for optimal hohlraum efficiency [39], nevertheless, it is not compatible with the non-proliferation requirements of a LIFE[1] power plant.

Recently, new candidate hohlraum materials like lead are examining by the ICF researchers with the aim of lower costs and minimum material use [40, 41].

In this paper, we investigate the effects of reducing the initial density on soft X-ray emission from laser-irradiated lead and gold targets as hohlraum wall materials. Numerical experiments are performed to calculate soft X-ray emissions and total yield enhancement under irradiation conditions relevant for ICF experiments. Corresponding opacities are also calculated and compared for both Au and Pb plasmas created by laser irradiation of targets with different initial densities (porosities).

2 Calculations

Laser–target interaction and plasma hydrodynamics are simulated by 1.5D (or quasi-2D) hydrodynamic/atomic code 'EHYBRID' [42]. The code uses 98 lagrangian cells for planner single- or multi-layer targets, and laser light is considered to normally irradiate the target surface.

The code calculates the time-dependent ionization using a collisional radiative model for one species and an optional steady-state average atom model for the others. Laser absorption occurs via inverse bremsstrahlung (and considers refraction), and resonant absorption is modeled by assuming a 30 % dump of the laser energy at the critical density. A flux limiter of 0.1 is included for the reduction

of energy transport from the free streaming limit. Plasma parameters are calculated in the same direction of the laser beam, and transverse expansion is considered to be self-similar. In the calculations, planar Au and Pb targets are considered with different initial densities as hohlraum wall materials. We know that the geometry of hohlraum is cylindrical; however, we are comparing the variation of X-ray emission from tow different materials in the conditions of solid or porous targets. Therefore, the geometry of the targets is not important in this study remarkably and has no considerable effect on the X-ray enhancement going from solid to porous targets conditions.

Targets are irradiated by 351-nm, 2-ns flat-top laser pulses with intensities of 10^{14} and 10^{15} W cm^{-2}. Such conditions are relevant for currently performing ignition experiments [43, 44]. By using the calculated plasma parameters such as temperature, density, and average ionization, continuum bremsstrahlung and recombination emissions were calculated for each simulation cell at each time step in the soft X-ray region (0.1–5 keV). With considering the corresponding plasma opacities, enhancement of total yields were calculated for both Au and Pb targets with various initial densities. Due to the computational complexity, line emission is not taken into account in the calculations and will be considered in our future study. However, it should be noted that a significant proportion of X-ray emission comes from continuum Bremsstrahlung and recombination radiations. Therefore, in this paper we examine these continuous radiations, in different circumstances.

Plasma continuum radiation comes from recombination and Bremsstrahlung emissions which can be generally derived from the corresponding cross sections. Considering a hydrogenic system, recombination of electrons to a bound state with principal quantum number n of the ions of charge Z results in emission coefficient or emissivity [45, 46]:

$$\eta_n^R(\nu)\mathrm{d}\nu = \frac{\hbar\omega}{4\pi}n_Z n_e \sigma_{\mathrm{vn}} f(\upsilon)\upsilon\mathrm{d}\upsilon, \tag{1}$$

in frequency interval dν into one sr. Here n_Z, n_e, σ_{vn}, and $f(\upsilon)$ are density of ions of charge Z, free electron density, free-bound cross section, and the electron velocity distribution, respectively.

It can be shown that relation (1) leads to the following relation for recombination emission [45–47]:

$$\eta_n^R(\nu)\mathrm{d}\nu = C n_Z n_e G_{\mathrm{fb}} Z^4 T_e^{-\frac{3}{2}} \frac{1}{n^3} \exp\left(-\frac{h\nu}{kT_e} + \frac{I_n^Z}{kT_e}\right)\mathrm{d}\nu, \tag{2}$$

where $C = 1.72 \times 10^{-46}$ in units J s^{-1} m^3 sr^{-1} Hz^{-1} K$^{3/2}$, I_n^Z is the ionization potential. G_{bf} is the photoionization Gaunt factor which is in fact the ratio of quantum mechanical to classical photo-cross section. This parameter varies slowly

---

[1] Laser Inertial Fusion Energy.

with v and is of order unity for most of practical interest [47]. One can obtain the total radiation in frequency interval $\mathrm{d}v$ by summing the values of relation (2) for all permitted quantum energy levels. Finally, the total monochromatic free-bound radiation in units w m^{-3} sr^{-1} Hz^{-1} is obtained as:

$$
\eta^R(v) = 1.72 \times 10^{-46}\, n_Z n_e G_{fb} Z^4 T_e^{-\frac{3}{2}} \exp\left(-\frac{hv}{kT_e}\right)
$$
$$
\times \left(\sum_{n \geq \left(\frac{Z^2 I_H}{hv}\right)^{1/2}}^{\infty} \frac{1}{n^3} \exp\left(\frac{I_n^Z}{kT_e}\right)\right). \tag{3}
$$

To calculate the recombination of electrons into free states or the so-called Bremsstrahlung emission, relation (3) can be used knowing that $I_n^Z < 0$ corresponds to the free continuous states. In such conditions, energy levels approach continuum and the summation can be replaced by an integral which results in:

$$
\eta^B(v)\mathrm{d}v = 1.72 \times 10^{-46} \frac{k}{2I_H} n_Z n_e G_{ff} Z^2 T_e^{-\frac{1}{2}} \exp\left(-\frac{hv}{kT_e}\right)\mathrm{d}v, \tag{4}
$$

where G_{fb} is replaced with the free–free Gaunt factor G_{ff}. Consequently, the total continuum emission in frequency interval $\mathrm{d}v$ due to free–free and free-bound radiations is:

$$
\eta(v)\mathrm{d}v = 1.72 \times 10^{-46}\, n_Z n_e \exp\left(-\frac{hv}{kT_e}\right)
$$
$$
\times \left[\frac{k}{2I_H} G_{ff} Z^2 T_e^{-\frac{1}{2}} + G_{fb} Z^4 T_e^{-\frac{3}{2}}\right.
$$
$$
\times \left.\left(\sum_{n \geq \left(\frac{Z^2 I_H}{hv}\right)^{1/2}}^{\infty} \frac{1}{n^3} \exp\left(\frac{I_n^Z}{kT_e}\right)\right)\right]\mathrm{d}v
$$
$$
\times \left(\mathrm{w} \cdot \mathrm{m}^{-3} \cdot \mathrm{sr}^{-1} \cdot \mathrm{Hz}^{-1}\right) \tag{5}
$$

To consider reabsorption of the emitted X-rays, radiative transfer equation should be considered. The transfer equation for a radiation of intensity I (J s^{-1} m^{-2} sr^{-1} Hz^{-1}) propagating along x direction, can be written as [48]:

$$
\frac{\mathrm{d}I(v,x)}{\mathrm{d}x} = -\kappa(v,x)I(v,x) + \eta(v,x), \tag{6}
$$

where, $\kappa(v,x)$ and $\eta(v,x)$ are the absorption and emission coefficients of the material at point x with units cm^{-1} and J s^{-1} m^{-3} sr^{-1} Hz^{-1}, respectively. X-ray absorption in the plasma can originate from four atomic processes: inverse Bremsstrahlung (free–free transitions), photoionization (bound-free transitions), line absorption (bound–bound transitions), and photon–electron scattering. The total absorption coefficient can be written as:

$$
\kappa(v,x) = \kappa_{ff} + \kappa_{bf} + \kappa_{bb} + \kappa_s. \tag{7}
$$

The thermally averaged free–free absorption at frequency v can be obtained from [49]:
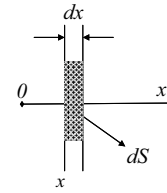

Fig. 1 Schematic description of the geometry of a plasma simulation cell

$$
\kappa_{ff} = \frac{\sqrt{2\pi}\,4e^6}{3\sqrt{3}\,h m_e^{3/2} c}(kT_e)^{-\frac{1}{2}} n_e n_Z Z^2 v^{-3} G_{ff}\left(1 - e^{-hv/kT_e}\right). \tag{8}
$$

The photoionization cross section for a ion of charge Z with a bound electron in a level with principal quantum number n can be written as [46, 47]:

$$
\sigma_v(n, Z) = \begin{cases} \frac{64\pi^4 m_e e^{10}}{3^{3/2} h^6 c} Z^4 \frac{1}{n^5} \frac{1}{v^3} G_{bf}, & \text{if } hv \geq I_n \\ 0, & \text{if } hv < I_n \end{cases}. \tag{9}
$$

It should be noted that (as is explained in the references) this relation is obtained with considering hydrogenic energy levels for the recombining ions.

Consequently, the absorption coefficient corresponding to photoionization from all permitted energy levels of ions of charge Z can be obtained as:

$$
\kappa_{bf} = \sum_{n \geq \left(\frac{Z^2 I_H}{hv}\right)^{1/2}}^{\infty} n_Z \sigma_v(n, Z)\left(1 - e^{-hv/kT_e}\right), \tag{10}
$$

where n_Z is the number density of ions of charge Z and the factor $\left(1 - e^{-hv/kT_e}\right)$ takes into account induced recombinations [50]. Photon–electron scattering is mostly accounted for by Thomson scattering by free electrons:

$$
\kappa_s = n_e \sigma_{Th}, \tag{11}
$$

and Thomson cross section is:

$$
\sigma_{Th} = \frac{8\pi e^4}{3me^2 c^4} = 6.65 \times 10^{-25} \text{ cm}^2 \tag{12}
$$

Using relations (8), (10), and (11), the total absorption coefficient can be obtained at each time step in each plasma cell. It must be noted that we are just dealing with continuum processes and bound–bound emission and that absorption is not considered in this study and will be considered in future works. Consider a planar simulation cell of the plasma with thickness $\mathrm{d}x$, area $\mathrm{d}S$, and volume $\mathrm{d}V = \mathrm{d}S\,\mathrm{d}x$ as is shown in Fig. 1.

In such conditions, variation of the radiation intensity after going through the plasma cell can be obtained from Eq. (6):

$$dI(\nu, x) = -\kappa(\nu, x)[I(\nu, x) - S(\nu, x)]dx, \qquad (13)$$

where $S(\nu, x) = \frac{\eta(\nu,x)}{\kappa(\nu,x)}$ is called the source function which is the ratio of emission to absorption coefficient having all the basic information about the plasma medium. Finally, by assuming uniform temperature and density in the plasma slab, the outcoming intensity can be obtained from:

$$I(\nu, x) = S(\nu, x)\left[1 - e^{-\kappa(\nu,x)dx}\right]. \qquad (14)$$

By summing over all plasma cells, the total continuum intensity can be calculated at each time step during and after laser radiation. A post-processor code was developed based on Eqs. (1)–(14) to calculate total continuum emission using plasma parameters obtained from EHYBRID.
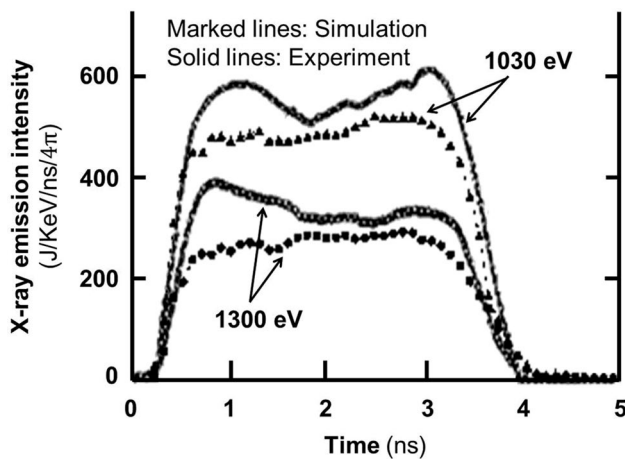

Fig. 2 Time dependence of X-ray intensity at two different photon energy for gold plasma. The Au target was irradiated by a 3-ns and 0.35-μm laser pulse of intensity 4.3×10^{14} W cm^{-2}. *Solid* and *marked lines* show the results from experiment and simulations, respectively

3 Results and discussion

To ensure realistic results, calculations were performed for the conditions of an experiment and the results were compared with the measured values. Figure 2 shows the emitted X-ray intensity measured over time for gold plasma created by a laser pulse of intensity 4.3×10^{14} W cm^{-2}, duration 3 ns and wavelength 0.35 μm [51]. We used the same parameters of the experiment (just for this figure) and compared our simulation results with those obtained experimentally to validate our calculation procedure. In the experiment, the time-dependent absolute emission intensity was measured with a spectrograph with six photon energy bands of 190, 280, 520, 790, 1030, and 1300 eV and channel bandwidths ≤150 eV. However, we used a channel bandwidth of 150 eV in the calculations. In Fig. 2, we just illustrate the results for two energy bands of 1030 and 1300 eV for comparison.

This figure shows that there is a relatively good agreement between the measured values and simulation results. It can be seen that a higher X-ray emission is obtained at lower photon energy (1030 eV). Little differences are observed between emission intensity plots obtained from simulations and experiment which can be resulted from two reasons. First, the laser beam was incident at 28° to the target normal in the experiment, while in EHYBRID code, the laser beam is considered to be perpendicular to the target surface. Secondly, as mentioned before, we are evaluating the continuum X-ray radiations in this study, but in the experimental data, total X-ray emission was measured containing the line X-ray emission.
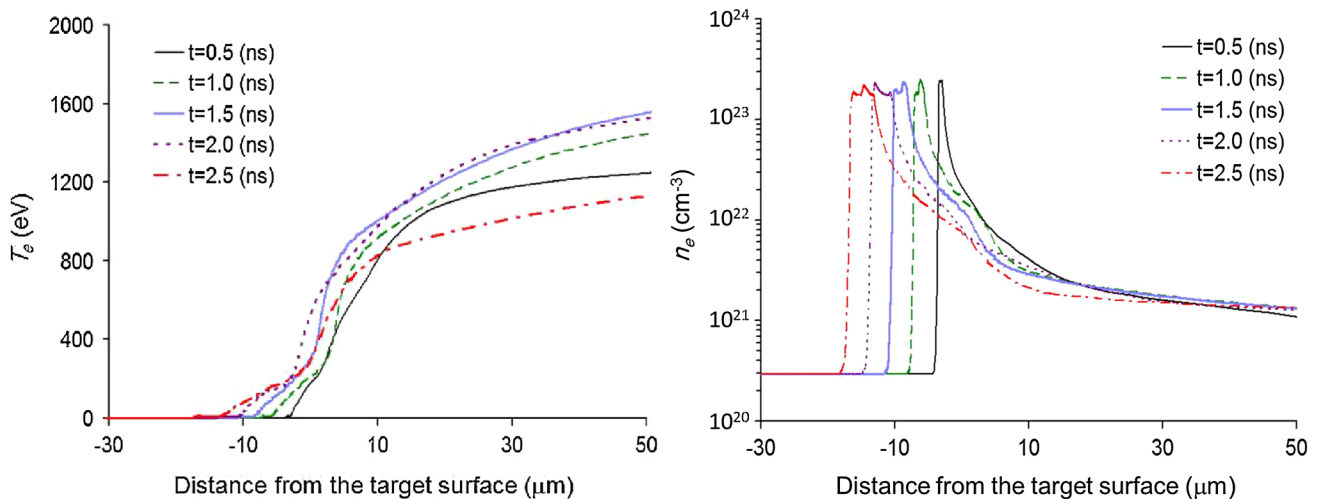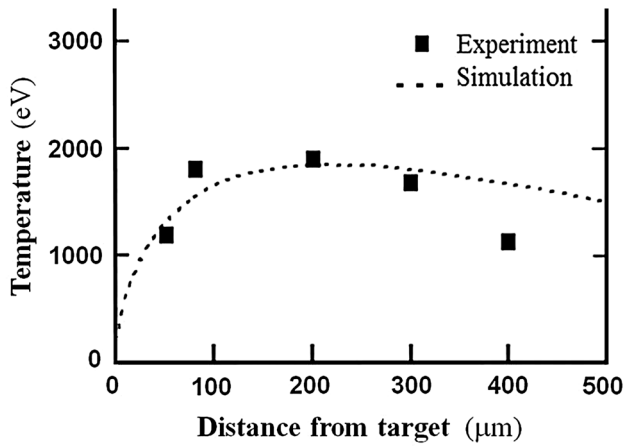

Fig. 3 Temperature and density distribution in Au plasma for several times during and after the laser pulse. The target is irradiated by a 2-ns laser pulse of intensity 10^{15} W cm^{-2} and wavelength 532 nm

Fig. 4 Measured and simulated electron temperature profile at the end of the laser pulse as a function of distance from the original target surface

3.1 Comparison of AU and Pb plasma properties

In order to have a proper view of the hydroevolutions of plasmas under consideration, variation of plasma parameters are calculated at different times during and after the laser pulse. Figure 3, for example, shows the results at several times for Au plasma produced by a 2-ns laser pulse of intensity 10^{15} W cm^{-2} and wavelength 532 nm. Zero point on the horizontal axis represents the initial position of the target surface. It can be seen that with increasing time, greater depth of the target is affected by the laser pulse, and electron temperature and density have increased in a more plasma volume. Obviously, the plasma temperature has increasing trend until the laser pulse is ended. Such behavior is also observed for Pb plasma.

It should be noted that in long-pulse regime as in our study, the produced plasma have enough time to expand and absorb a considerable fraction of the laser energy resulting in electron temperatures higher than 1 keV. To validate this temperature range, we calculated plasma parameters for the conditions of several published reports including measured and simulated results [52, 53]. Our results showed a good agreement with them. For example, Fig. 4 shows a comparison between the measured electron temperature reported by Chambers et al. [52] and our simulation results for the same experimental conditions. In this experiment, an aluminum target with thickness 1 μm was irradiated by a 1 ns (FWHM) trapezoidal pulse of intensity 3.5×10^{14} W cm^{-2} and wavelength 1.06 μm. Note that we are using these conditions just in Fig. 4 to validate temperatures greater than 1 keV. In this figure, electron temperature profiles obtained from both experiment and simulation at the end of the laser pulse are illustrated as a function of distance from the original target surface. It can be seen that there is a good agreement between measured and simulated results.

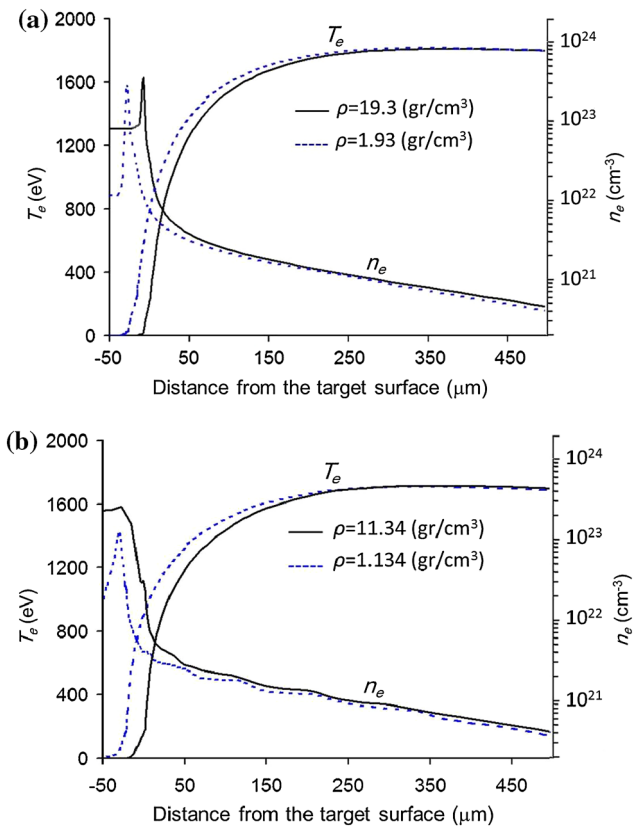It is desirable to see the effects of reducing initial mass density of the targets on various plasma parameters.

Fig. 5 Evolution of the free electron density and temperature across **a** Au and **b** Pb plasmas after 1.5-ns irradiation by 2-ns laser pulse of intensity 10^{15} W cm^{-2}. The results are shown for two different initial densities

Figure 5 shows electron density and temperature profiles across the plasmas produced by irradiating 50 μm Au and Pb planar targets of two different initial densities. The irradiation conditions are like Fig. 3. Calculations were performed for different times during and after the laser pulse. Here, we just present the results for the time 1.5 ns after the beginning of the driver pulse at which, a proper plasma volume with high temperature and density is created (see Fig. 3). Similar results are also observed at other times.

These figures show that by reducing initial densities to 0.1 of the solid density, a more depth of both materials is heated by the laser pulse. However, for both initial densities, a more thickness of Pb target is affected in comparison with Au target. The maximum plasma temperature is a little higher for gold plasma (about 1850 eV for Au and 1760 eV for Pb). Also it is observed that except in cold depths, Au plasma has a higher free electron density for both solid and porous targets.

This is very important especially just above the critical density (~8.9×10^{22} cm^{-3} for the conditions utilized here) from which most of X-rays come. Such conditions lead to higher X-ray yield for Au plasma as will be presented in
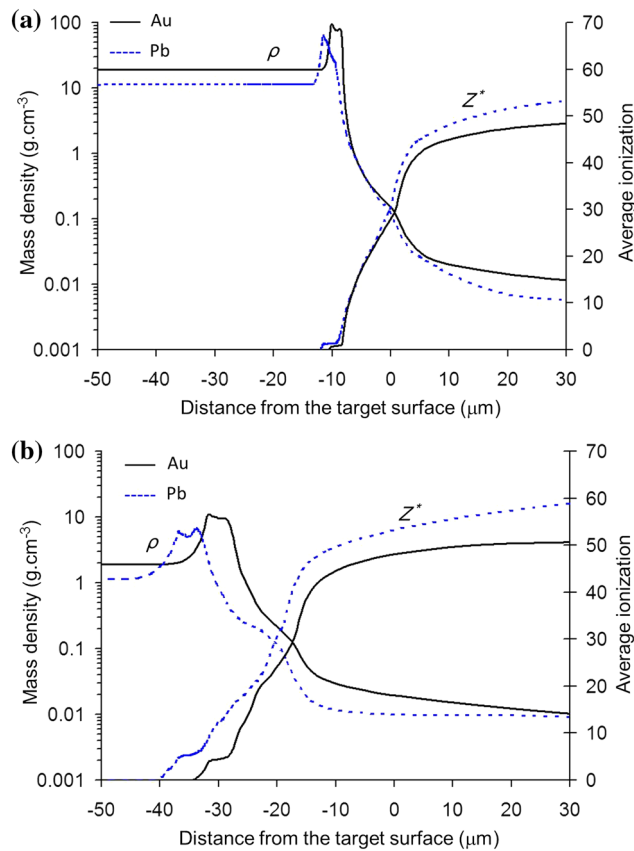
(a)

(b)

Fig. 6 Spatial dependence of average ionization and mass density for Au and Pb plasmas created from targets with initial densities equal to **a** solid densities and **b** 0.1 of the corresponding solid densities. Irradiation conditions are similar to those of Fig. 3

Fig. 7 Continuum X-ray spectrum due to bremsstrahlung (η_B) and recombination (η_R) emissivities for Pb plasma with $T_e = 1760$ eV and $n_e = 2.44 \times 10^{20}$ cm^{-3}

the next sections. Spatial variation of two other important plasma parameters, average ionization (Z^*) and mass density (ρ), is illustrated in Fig. 6. The results are shown for solid Au and Pb targets as well as porous targets with initial densities equal to 0.1 of the corresponding solid densities.

By comparing Fig. 6a, b, it can be deduced that by reducing the initial densities, more cells of both targets are ionized and also average ionization is increased to higher values which can be a result of the temperature increase as shown in Fig. 5. The lead plasma exhibits higher ionization, and a more volume of the lead target is affected by the laser beam because of its lower mass density. Moreover, as mentioned before, high-*Z*, low-density materials are desirable because of their lower energy loss. Therefore, lower density of the lead, especially above the critical surface, can lead to decreased hohlraum wall losses.

3.2 Plasma emission and opacity

A post-processor code was developed using relations given in previous sections to calculate plasma emission and

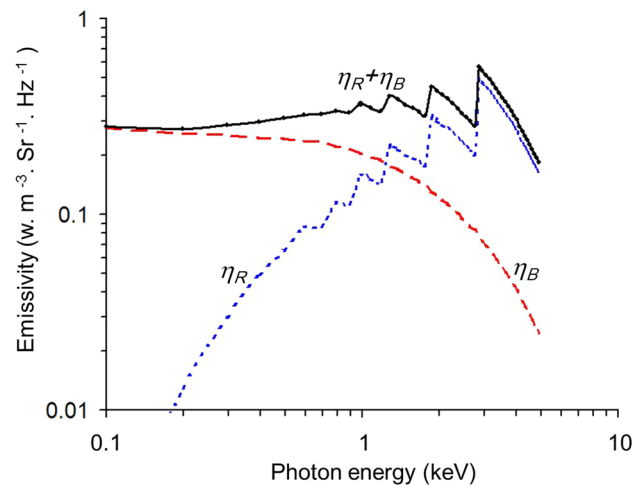absorption coefficients. Extracting plasma parameters from EHYBRID output and putting them as inputs of the post-processor code, soft X-ray emission was calculated at each time step in the expanding plasma cells. Numerical experiments were performed for both gold and lead targets with different initial mass densities. For a typical case, calculated Bremsstrahlung and recombination radiations from Pb plasma with $T_e = 1760$ eV and $n_e = 2.44 \times 10^{20}$ cm^{-3} with considering corresponding opacities are illustrated in Fig. 7. Initial density of the target was considered to be 1.134 g cm^{-3}, and other irradiation conditions are the same as Fig. 3.

It can be seen that for photon energies higher than about 1 keV, recombination dominates Bremsstrahlung radiation. At low energies, the total spectrum has a flat response which almost completely arises from Bremsstrahlung. At higher photon energies, the spectrum has a step-like structure because of recombination of electrons to different energy levels.

To study the effects of using porous targets instead of solid ones, calculations are performed for various initial densities, e.g., 1, 0.1, 0.01, and 0.005 of material's solid densities. Figure 8 shows temporal behavior of the total continuum X-ray intensity emitted from Au and Pb targets with different initial densities. It can be seen that in all conditions, X-ray emission curves have increasing trend with time until the driver pulse is turned off. X-ray emission is a little higher in the condition of Au; however, comparison of Fig. 8a, b reveals that X-ray yield can be enhanced by decreasing initial densities for both Au and Pb targets in a similar manner.

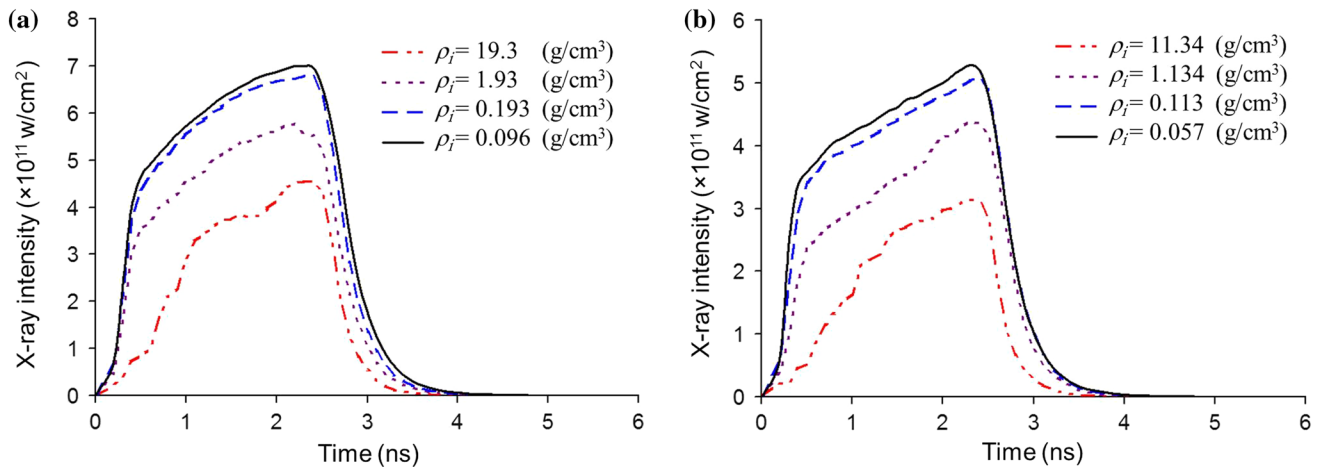As was shown in the previous section, reducing initial density causes the laser pulse to interact more

(a)

(b)

Fig. 8 Temporal evolution of total continuum emission from **a** Gold and **b** Lead targets with different initial densities irradiated by a laser pulse of the same conditions used in Fig. 3

effectively with the target. As a result, laser energy absorption increases leading to more desirable values of hydrodynamic variables such as temperature, density and ionization as can be seen in Figs. 5 and 6. Finally, in such conditions, X-ray emission in the corresponding photon energy range is considerably increased by reducing initial densities of both targets.

The total X-ray yield emitted from each target can be calculated by integrating the emissivity over time and frequency (or photon energy range of 0.1–5 keV) and then summing the obtained values for all plasma cells. Figure 9 shows the dependence of X-ray yield enhancement to the density ratio of the target. The density ratio is defined as ρ_i/ρ_s in which ρ_s is the solid material density. In this figure, the yields are normalized with respect to the value of solid density material with $\rho_i/\rho_s = 1$.

From this figure, it is clear that total X-ray yields have increasing trend with decreasing initial ratios for both gold and lead targets. It should be noted that at the same density ratios, total yields from Au plasma is higher than those of Pb plasma; however, the value of X-ray enhancement, caused by reduced density ratio, is greater in the conditions of Pb target. For example, at $\rho_i/\rho_s = 1$, the value of total yield for Au target is about 1.5 times greater than that of Pb target. By decreasing density ratio to $\rho_i/\rho_s = 0.1$, an enhancement of 1.3 is obtained for Au, while for the Pb target the enhancement is about 1.53. These results mean that we can obtain the same X-ray yield even more by using Pb target of density ratio $\rho_i/\rho_s = 0.1$ instead of solid Au target. Therefore, in the following, we consider this density ratio for our porous Pb target to provide a comparison between emissivity and opacity properties of solid Au and porous Pb targets. Obviously, according to Fig. 9, lower density ratio values can give even higher increases in the X-ray yield.
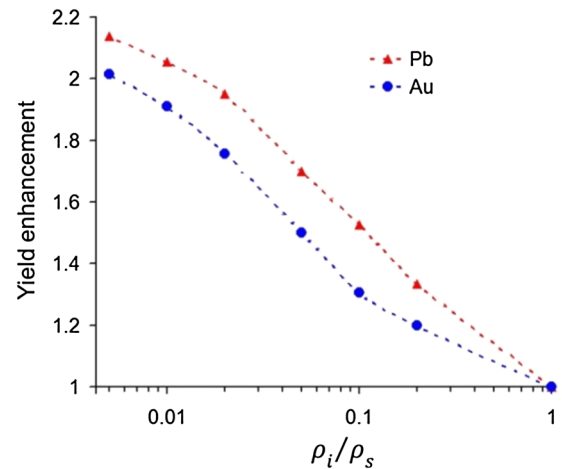

Fig. 9 Enhancement of X-ray yield with respect to target's density ratio. Total yields are normalized to the values obtained for solid density targets

Figure 10 shows X-ray yields produced in plasma cells of Au and Pb targets with two different initial densities. Simulation results for two laser intensities of 10^{14} and 10^{15} W cm^{-2} are presented in Fig. 10a, b, respectively. It can be deduced from these figures that for both laser intensities, X-ray emission from Au plasma is higher for both selected initial densities. By decreasing initial densities, more cells are affected by the laser beam, and therefore, more considerable cells participate in X-ray emission. In fact, for targets with lower initial densities, the plasma critical density occurs in dipper cells leading to higher absorption of laser energy and a more emitting plasma volume. Calculation of total yields in these conditions also showed that for both laser
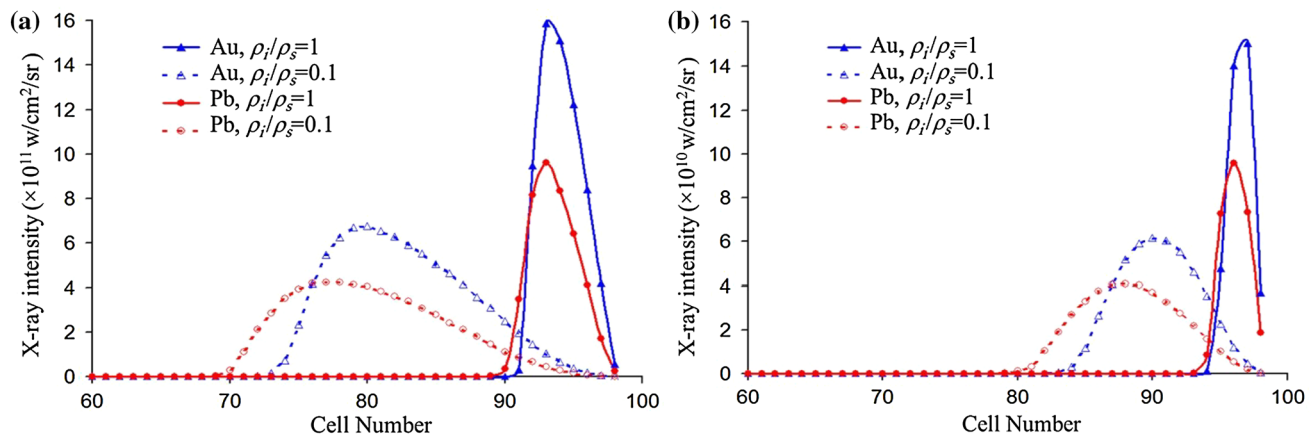
Fig. 10 Time-integrated X-ray emitted from plasma cells of Au and Pb targets with density ratios of 1 and 0.1 for laser intensities of **a** 10^{15} and **b** 10^{14} W cm^{-2}
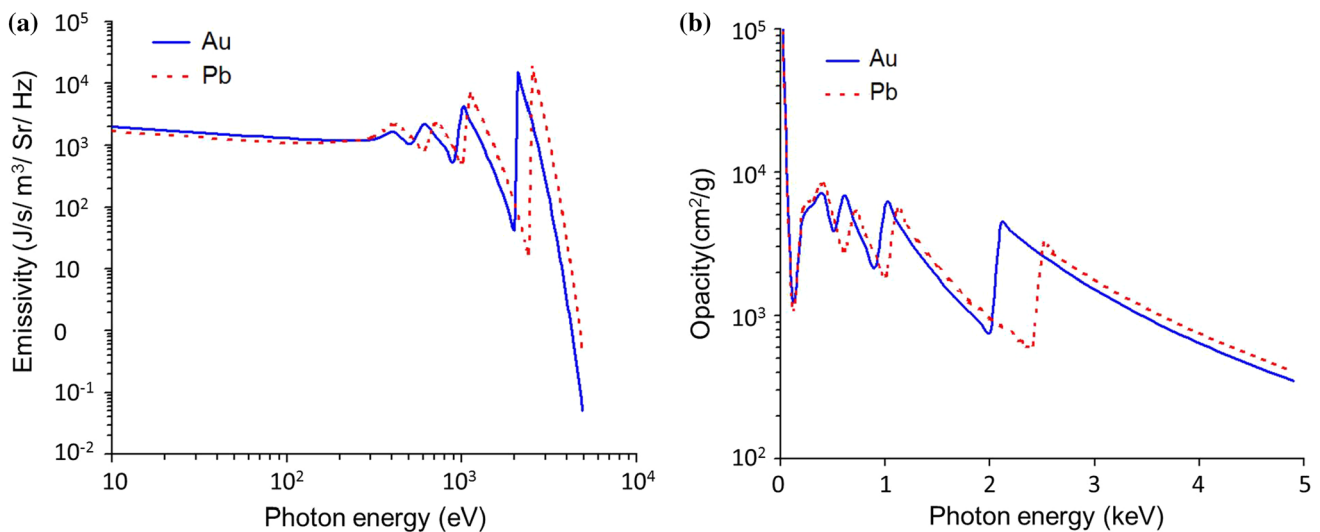

Fig. 11 **a** X-ray emissivity and **b** opacity of Au and Pb laser produced plasmas at $T_e = 220$ eV and $\rho = 0.2$ g cm^{-3}

intensities, the value of X-ray enhancement is greater for Pb target.

Opacity of the material in the X-ray region is a key property which plays an important role in choosing appropriate hohlraum materials. More specifically, the effect of opacity becomes very important above the critical density toward the target bottom where it can help to reduce energy losses in hohlraum wall. It is desirable to study the opacity and emissivity behavior for both Au and Pb targets in this region. To have a better comparison, we searched the cells at time 1.5 ns and selected the ones which were in the mentioned region and also had approximately equal values of temperature and mass density in both targets. Here, we just present the results for one of such plasma cells of both targets with temperature 220 eV and mass density

0.2 g cm^{-3}, for example. Frequency-dependent X-ray emission and absorption at the selected plasma temperature and density are illustrated in Fig. 11a, b, respectively. In these figures, a little difference can be observed in both emission and absorption spectrums of Au and Pb. These differences at equal temperature and mass density conditions can be attributed to the Z dependence of emission and absorption coefficients. In such conditions, Pb ions are in a little higher ionization states in comparison with Au plasma as can be seen in Fig. 6. Also such conditions lead to "jumps" to occur at higher energies in Pb spectrums.

Since the maximum X-ray emission comes from just above the critical density, therefore, we calculated plasma opacity at two selected plasma cells above the critical surface. Calculations are performed for Au and Pb targets
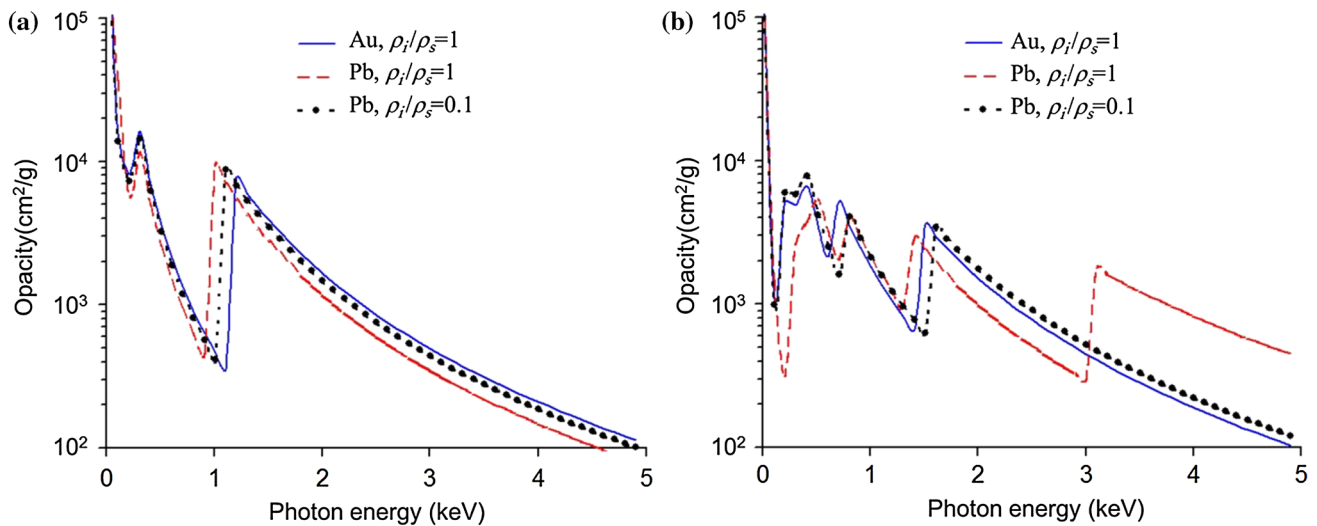
Fig. 12 Au and Pb plasma opacities at temperatures **a** 50 and **b** 160 eV and electron densities above the critical

with density ratios of 1 and 0.1 at time 1.5 ns during laser irradiation.

Here, too, we selected those cells of the targets which were in the proper region (above the critical density toward the target bottom) having approximately equal temperatures, after 1.5-ns laser irradiation. For a better comparison, the results are presented for two cells having such conditions in the targets under study. These cells were found to have temperatures about 50 and 160 eV and densities about 2.75×10^{23} and 9.1×10^{22} cm^{-3}, respectively. It must be noted that for experimental conditions considered in this study, the critical density is about 8.9×10^{22} cm^{-3}. The results are presented in Fig. 12. It can be seen from Fig. 12a that at 50 eV, solid Pb target has a lower opacity; however, by decreasing the density ratio, its opacity increases and approaches to that of Au plasma. Closer to the critical surface at temperature 160 eV (Fig. 12b), solid Pb plasma has still lower opacity until about photon energy 3 keV at which a jump is observed. This jump (which corresponds to recombination of electrons into a different shell) is a result of higher average ionization of solid Pb plasma in comparison with porous Pb and solid Au. These figures reveals that decreasing the initial density of Pb targets causes its opacity to increase and get closer to the opacity of solid Au which in turn reduce energy losses in hohlraum wall.

4 Conclusions

Continuum soft X-ray emissions and also corresponding opacities were calculated for laser-irradiated gold and lead targets as hohlraum wall materials, and the results were compared in details. Numerical experiments were performed for different initial densities (or different porosities) of the targets. The results show that under identical irradiation conditions, X-ray emission is a little higher for Au. By reducing initial densities, total X-ray yields were enhanced for both targets; however, yield enhancement (with respect to those of solid targets) was greater for Pb. Calculations showed that nearly the same yield can be obtained in the conditions of solid Au target or Pb target of density ratio 0.1. Opacity calculations also showed that solid Pb plasma has a little lower opacity in comparison with solid Au plasma in most parts of the soft X-ray wavelength region. By decreasing Pb initial density, its opacity was increased and got so closed to the value of the solid Au plasma at a density ratio of 0.1. Finally, with regards to favorable characteristics of X-ray emissivity and opacity of Pb plasma, it can be concluded that lead can be a good substitute for gold as hohlraum material especially with initial densities less than solid. This result is so critical in new hohlraum designs with the aim of significantly reducing costs. It should be noted that in these calculations, line emission is not taken into account and will be considered in a future work. However, in a previous study we showed that line emission can also be increased by reducing initial density of the laser-irradiated target [36].

References

1. J.H. Gardner, A.J. Schmitt, J.P. Dahlburg, C.J. Pawley, S.E. Bodner, S.P. Obenschain, V. Serlin, Y. Aglitskiy, Phys. Plasmas **5**, 1935 (1998)
2. S.H. Glenzer, B.J. MacGowan, P. Miche, N.B. Meezan, L.J. Suter, S.N. Dixit, J.L. Kline, G.A. Kyrala, D.K. Bradley, D.A. Callahan, E.L. Dewald, L. Divol, E. Dzenitis, M.J. Edwards,

A.V. Hamza, C.A. Haynam, D.E. Hinkel, D.H. Kalantar, J.D. Kilkenny, O.L. Landen, J.D. Lindl, S. LePape, J.D. Moody, A. Nikroo, T. Parham, M.B. Schneider, R.P.J. Town, P. Wegner, K. Widmann, P. Whitman, B.K.F. Young, B. Van Wonterghem, L.J. Atherton, E.I. Moses, Science **327**, 1228 (2010)

3. J.D. Lindl, P. Amendt, R.L. Berger, S.G. Glendinning, S.H. Glenzer, S.W. Haan, R.L. Kauffman, O.L. Landen, L.J. Suter, Phys. Plasmas **11**, 339 (2004)

4. M. Cable, S.P. Hatchett, J.A. Caird, J.D. Kilkenny, H.N. Kornblum, S.M. Lane, C. Laumann, R.A. Lerche, T.J. Murphy, J. Murray, M.B. Nelson, D.W. Phillion, H. Powell, D.B. Ress, Phys. Rev. Lett. **73**, 2316 (1994)

5. J.D. Lindl, *Inertial Confinement Fusion* (Springer, New York, 1998)

6. J.D. Lindl, Phys. Plasmas **2**, 3933 (1995)

7. E. Dattolo, L. Suter, M.C. Monteil, J.P. Jadaud, N. Dague, S. Glenzer, R. Turner, D. Juraszek, B. Lasinski, C. Decker, O. Landen, B. MacGowan, Phys. Plasmas **8**, 260 (2001)

8. N.D. Delamater, E.L. Lindman, G.R. Magelssen, B.H. Failor, T.J. Murphy, A.A. Hauer, P. Gobby, J.B. Moore, V. Gomez, K. Gifford, R.L. Kauffman, O.L. Landen, B.A. Hammel, G. Glendinning, L.V. Powers, L.J. Suter, S. Dixit, R.R. Peterson, A.L. Richard, Phys. Plasmas **7**, 1609 (2000)

9. S.G. Glendinning, S.V. Weber, P. Bell, L.B. DaSilva, S.N. Dixit, M.A. Henesian, D.R. Kania, J.D. Kilkenny, H.T. Powell, R.J. Wallace, P.J. Wegner, J.P. Knauer, C.P. Verdon, Phys. Rev. Lett. **69**, 1201 (1992)

10. S.H. Glenzer, L.J. Suter, R.L. Berger, K.G. Estabrook, B.A. Hammel, R.L. Kauffman, R.K. Kirkwood, B.J. MacGowan, J.D. Moody, J.E. Rothenberg, R.E. Turner, Phys. Plasmas **7**, 2585 (2000)

11. S.W. Haan, S.M. Pollaine, J.D. Lindl, L.J. Suter, R.L. Berger, L.V. Powers, W.E. Alley, P.A. Amendt, J.A. Futterman, W.K. Levedahl, M.D. Rosen, D.P. Rowley, R.A. Sacks, A.I. Shestakov, G.L. Strobel, M. Tabak, S.V. Weber, G.B. Zimmerman, W.J. Krauser, D.C. Wilson, S.V. Coggeshall, D.B. Harris, N.M. Hoffman, B.H. Wilde, Phys. Plasmas **2**, 2480 (1995)

12. R.L. Kauffman, L.V. Powers, S.N. Dixit, S.G. Glendinning, S.H. Glenzer, R.K. Kirkwood, O.L. Landen, B.J. MacGowan, J.D. Moody, T.J. Orzechowski, D.M. Pennington, G.F. Stone, L.J. Suter, R.E. Turner, T.L. Weiland, A.L. Richard, M.A. Blain, Phys. Plasmas **5**, 1927 (1998)

13. O. L. Landen, P. A. Amendt, R. E. Turner, S. G. Glendinning, D. H. Kalantar, C. D. Decker, L. J. Suter, M. D. Cable, R. Wallace, B. A. Hammel, J. D. Kilkenny, D. Bradley, F. J. Marshall, R. Keck, R. Kremens, W. Seka, J. Schnittman, R. Craxton, C. P. Verdon, J. Soures, R. McCrory, T. J. Murphy, N. Delamater, J. Wallace, C. Barnes, G. Magelssen, P. Gobby, A. Hauer, N. Dague, A. Richard, J. P. Jadaud, in *Proceedings of the IAEA*, Osaka (1998)

14. B. J. MacGowan, R. L. Berger, B. I. Cohen, C. D. Decker, S. Dixit, S. H. Glenzer, D. E. Hinkel, R. K. Kirkwood, A. B. Langdon, E. Lefebvre, J. D. Moody, J. E. Rothenberg, C. Rousseaux, L. J. Suter, C. H. Still, E. A. Williams, in *Proceedings of the IAEA*, Yokahama (1999)

15. M. D. Rosen, J. D. Lindl, *Laser Program Annual Report*, Lawrence Livermore National Laboratory, Livermore, CA, UCRL-50055-83, 1983 (unpublished)

16. R.P.J. Town, A.R. Bell, Phys. Rev. Lett. **67**, 1863 (1991)

17. H.X. Vu, Comput. Phys. Commun. **127**, 71 (2000)

18. G.B. Zimmerman, W.L. Kruer, Comments Plasma Phys. Control. Fusion **2**, 51 (1975)

19. B.A. Remington, S.V. Weber, M.M. Marinak, S.W. Haar, J.D. Kilkenny, R. Wallace, G. Dimonte, Phys. Rev. Lett. **73**, 545 (1994)

20. T.J. Orzechowski, M.D. Rosen, H.N. Kornblum, J.L. Porter, L.J. Suter, A.R. Thiessen, R.J. Wallace, Phys. Rev. Lett. **77**, 3545 (1996)

21. D. Colombant, M. Klapisch, A. Bar-Shalom, Phys. Rev. E **57**, 3411 (1998)

22. L. Suter, J. Rothenberg, D. Munro, B. Van Wonterghem, S. Haan, Phys. Plasmas **7**, 2092 (2000)

23. H.L. Wilkens, J. Gunther, M.P. Mauldin, A. Nikroo, J.R. Wall, D.R. Wall, R.J. Wallace, Fusion Sci. Technol. **49**, 846 (2006)

24. H.L. Wilkens, A. Nikroo, D.R. Wall, J.R. Wall, Phys. Plasmas **14**, 056310 (2007)

25. O.S. Jones, J. Schein, M.D. Rosen, L.J. Suter, R.J. Wallace, E.L. Dewald, S.H. Glenzer, K.M. Campbell, J. Gunther, B.A. Hammel, O.L. Landen, C.M. Sorce, R.E. Olson, G.A. Rochau, H.L. Wilkens, J.L. Kaae, J.D. Kilkenny, A. Nikroo, S.P. Regan, Phys. Plasmas **14**, 056311 (2007)

26. J. Schein, O. Jones, M. Rosen, E. Dewald, S. Glenzer, J. Gunther, B. Hammel, O. Landen, L. Suter, R. Wallace, Phys. Rev. Lett. **98**, 175003 (2007)

27. M.D. Rosen, J.H. Hammer, Phys. Rev. E **72**, 056403 (2005)

28. A.A. Andreev, J. Limpouch, A.B. Iskakov, H. Nakano, Phys. Rev. E **65**, 026403 (2002)

29. W. Mead, E.K. Stover, Phys. Rev. A **38**, 5275 (1988)

30. G. Kulcsár, D. AlMawlawi, F.W. Budnik, P.R. Herman, M. Moskovits, L. Zhao, R.S. Marjoribanks, Phys. Rev. Lett. **84**, 5149 (2000)

31. P.P. Rajeev, P. Ayyub, S. Bagchi, G.R. Kumar, Opt. Lett. **29**, 2662 (2004)

32. T. Nishikawa, H. Nakano, K. Oguri, N. Uesugi, K. Nishio, H. Masuda, J. Appl. Phys. **96**, 7537 (2004)

33. T. Nishikawa, H. Nakano, N. Uesugi, T. Serikawa, Appl. Phys. B **66**, 567 (1998)

34. H. Nakano, A.A. Andreev, J. Limpouch, Appl. Phys. B **79**, 469 (2004)

35. R. Fazeli, M.H. Mahdieh, G.J. Tallents, Phys. Lett. A **374**, 2936 (2010)

36. R. Fazeli, M.H. Mahdieh, G.J. Tallents, Laser Part. Beams **29**, 193 (2011)

37. H. Nishimura, T. Endo, H. Shiraga, Y. Kato, S. Nakai, Appl. Phys. Lett. **62**, 1344 (1992)

38. H. Fiedorowicz, A. Bartnik, R. Jarocki, R. Rakowski, M. Szczurek, Appl. Phys. B **70**, 305 (2000)

39. P. Amendt, M. Dunne, D.D. Ho, J.D. Lindl, Fusion Sci. Technol. **60**, 49 (2011)

40. M. Dunne, E.I. Moses, P. Amendt, T. Anklam, A. Bayramian, E. Bliss, B. Debs, R. Deri, T. Diaz de la Rubia, B. El-Dasher, J.C. Farmer, D. Flowers, K.J. Kramer, L. Lagin, J.F. Latkowski, J. Lindl, W. Meier, R. Miles, G.A. Moses, S. Reyes, V. Roberts, R. Sawicki, M. Spaeth, E. Storm, Fusion Sci. Technol. **60**, 19 (2011)

41. J.S. Ross, P. Amendt, L.J. Atherton, M. Dunne, S.H. Glenzer, J.D. Lindl, D. Meeker, E.I. Moses, A. Nikroo, R. Wallace, Sci. Rep. **3**, 1453 (2013)

42. G.J. Pert, J. Fluid Mech. **131**, 401 (1983)

43. E.L. Dewald, M. Rosen, S.H. Glenzer, L.J. Suter, F. Girard, J.P. Jadaud, J. Schein, C. Constantin, F. Wagon, G. Huser, P. Neumayer, O.L. Landen, Phys. Plasmas **15**, 072706 (2008)

44. R.E. Olson, L.J. Suter, J.L. Kline, D.A. Callahan, M.D. Rosen, K. Widmann, E.A. Williams, D.E. Hinkel, N.B. Meezan, G.A. Rochau, A.L. Warrick, S.H. Langer, C. Thomas, S.N. Dixit, E.L. Dewald, M.B. Schneider, J.D. Moody, P. Michel, R.J. Wallace, O.L. Landen, J. Edwards, B.J. MacGowan, S.H. Glenzer, J. Phys: Conf. Ser. **244**, 032057 (2010)

45. H.R. Griem, *Plasma Spectroscopy* (McGraw-Hill, New York, 1964)

46. J. Cooper, Rep. Prog. Phys. **29**, 35 (1966)

47. W.J. Karzas, R. Latter, Astrophys. J. Suppl. VI **55**, 167 (1961)

48. S. Chandrasekhar, *Radiative Transfer* (Dover, New York, 1950)

49. D. Salzmann, *Atomic Physics In Hot Plasmas* (Oxford University Press, Oxford, 1998)
50. D. Mihalas, *Stellar Atmospheres* (W. H. Freeman, 1978)
51. F. Ze, D.R. Kania, S.H. Langer, H. Kornblum, R. Kauffman, J. Kilkenny, E.M. Campbell, G. Tietbohl, J. Appl. Phys. **66**, 1935 (1989)
52. D.M. Chambers, S.H. Glenzer, J. Hawreliak, E. Wolfrum, A. Gouveia, R.W. Lee, R.S. Marjoribanks, O. Renner, P. Sondhauss, S. Topping, P.E. Young, P.A. Pinto, J.S. Wark, JQSRT **71**, 237 (2001)
53. A. Djaoui, R. Evans, T.A. Hall, A. Badger, F.B. Rosmej, J. Phys. B: At. Mol. Opt. Phys. **28**, 1921 (1995)